EAI Endorsed Transactions
on AI and Robotics

EAI.EU Technical Article

Localization of the work coordinate system using computer vision and geometric transformations on three-axis CNC milling machines

MERAZ MÉNDEZ Manuel[1], DUARTE LOERA Jorge[1], LERMA HERNANDEZ Claudia[2]

[1]Industrial Maintenance Engineering at the Technological University of Chihuahua (UTCH), Mexico
[2]Industrial Engineering at the Polytechnic University of Chihuahua (UPCH), Mexico

Abstract

This paper presents a novel methodology for locating the workpiece coordinate system origin (WCS) on three-axis computer numerical control (CNC) milling machines. The proposed approach uses computer vision techniques to detect geometric features on the workpiece and calculates zero-point coordinates through pixel-based adjustment and coordinate transformation matrices. The method includes a calibration process to align the camera system with the machine's coordinate reference frames and compensates for displacement between the vision sensor and the tool center point. Experimental validation was carried out on a HAAS VF1 CNC milling machine, comparing the proposed method with traditional probing techniques. The results demonstrate improved repeatability and accuracy in the location of the WCS, with deviations maintained within acceptable industrial tolerances. This approach facilitates faster setup times and improves process automation in intelligent manufacturing environments.

Received on 07 August 2025; accepted on 02 September 2025; published on 19 September 2025

Keywords: milling, work coordinate system, repeatability, computer vision, geometric transformations, optimization

doi:10.4108/airo.9898

1. Introduction

The location of WCS is a crucial process in the initial configuration of the CNC machining. [1] defines it as the procedure for activating the reference system corresponding to the zero workpiece, which the programmer defines based on the manufacturing blueprint on a rigid piece arbitrarily fixed to the machine table CNC. The procedure consists of transferring the machine control origins, which are the coordinates of the zero workpiece relative to the zero machine coordinate system (MCS), using a set of coordinates measured at any point on the reference surfaces of the piece as defined by the programmer. This procedure establishes an optimal spatial relationship between WCS and MCS, ensuring a unique and precise orientation.

During the past decade, driven by the need to automate various processes in robotics and manufacturing, researchers such as [2], [3], [4], and [5] have conducted studies on the location of WCS. According to studies by [6] and [7], more than 30% errors are caused by human factors and operational methods. [8] indicates that most operational errors are due to inadequate location of the workpiece, caused by programming errors, blueprint interpretation errors, clamping method errors, cutting parameter calculation errors, and machine operation errors. Based on this, [9] conclude that if these issues are not addressed, they will significantly impact the accuracy and repeatability of part manufacturing, which makes it essential to resolve them to optimize machining processes.

Traditionally, locating the WCS of the workpiece on a workstation requires the interaction of a skilled operator to achieve high precision clamping and positioning. Today, different devices are available on the market to facilitate this process. In some cases, the location of the WCS of the workpiece may take several minutes, whereas the machining process can sometimes take even fewer minutes. This

*Corresponding author. Email: mmeraz@utch.edu.mx

challenge underscores the importance of improving and automating workpiece location to enhance efficiency and reduce costs in manufacturing processes.

In studies conducted by [10], critical errors in the location of *WCS* in the workpiece process were identified to be primarily human-derived and arise due to factors such as lack of experience and training, errors in machine handling, difficulties in interpreting blueprints and work instructions, problems in selecting and calibrating cutting tools, difficulty in determining appropriate clamping methods, setting optimal cutting parameters (cutting speed, feed rate, depth, cooling, manufacturing sequence) and defining start points of the task. Therefore, according to research by [9], errors in locating the workpiece *WCS* can lead to negative consequences such as downtime, poor machine performance, unwanted dimensional variations, geometric errors, and reduced tool life, among other issues.

In studies conducted by [1], [11] and [12], it was established that one of the most frequently occurring errors is the location of the workpiece *WCS* and the calibration of the tools, which together represent 40% of the total problems to be addressed. In their analysis of machining errors, [13] and [14] demonstrated that locating the workpiece *WCS* is a time-consuming operation prone to errors, particularly in small-batch production, custom components, and large or complex shapes. However, in mass production, significant downtime accumulates due to this, which is why [15] and [16] recommend that the proper location of the workpiece *WCS* on the machine tool is vital to reduce errors.

Based on laboratory studies and tests, [13] demonstrated that the location of the workpiece *WCS* is an operation that consumes more than 15 minutes, because adjustments are required during the installation of the workpiece and the calibration of the cutting tools to be used. As a consequence, [17] determined that to improve the precision of the machining, it is essential to perform a proper preparation of the machine tools, including: the calibration of cutting tools, the calculation of the machining parameters, the sequencing of operations, and the installation of the clamping elements of the workpiece. Moreover, the location of the workpiece *WCS* requires specialized and well-trained personnel to minimize human errors. On the other hand, [10] stated that human errors in machining production processes lead to deviations that do not meet established tolerances due to actions not followed properly by operators. For this reason, [18] analyzed the factors influencing human errors in modern manufacturing processes and determined that one of the main causes is the incorrect location of the coordinates of the workpiece *WCS*.

2. Theoretical background

2.1. Geometric Transformations Applied to Images

[19] states that a geometric transformation applied to an image involves changing the positions of pixels when an image changes position. [20] asserts that this transformation can involve translation, rotation, or scaling. [21]mentions that homogeneous transformation matrices are used for translation, rotation, and scaling, as explained below:

Translation If a point P_a is defined in a coordinate system with coordinates X_a and Y_a, and is represented by the matrix P_a (1), then applying a translation vector t (2) results in a new point P_b as illustrated in Figure 1. According to [22], this transformation yields the coordinates of the point P_b, obtained by adding the translation components t_x and t_y to the original coordinates described in equation (3).

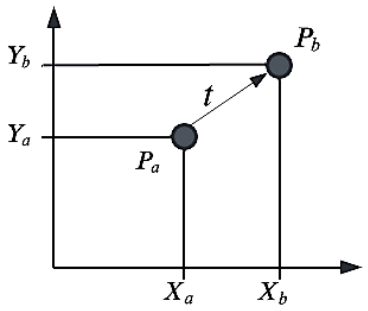

Figure 1. Translation from point P_a to point P_b

$$P_a = \begin{bmatrix} X_a \\ Y_a \end{bmatrix} \tag{1}$$

$$t = \begin{bmatrix} t_x \\ t_y \end{bmatrix} \tag{2}$$

$$X_b = X_a + t_x \qquad Y_b = Y_a + t_y \tag{3}$$

In general, this arrangement is defined as a geometric transformation expressed as $T\{P_a\} \rightarrow P_b$, and this operation is written in a translation matrix (4):

$$\begin{bmatrix} X_b \\ Y_b \\ 1 \end{bmatrix} = \begin{bmatrix} 1 & 0 & t_x \\ 0 & 1 & t_y \\ 0 & 0 & 1 \end{bmatrix} \begin{bmatrix} X_a \\ Y_a \\ 1 \end{bmatrix} \tag{4}$$

where X_a, Y_a are the coordinates of the point a, t_x and t_y are the components of the translation vector and X_b, Y_b are the final coordinates of the translated point b.

Rotation consists of rotating all the points of a figure around a center of rotation, applying a specific rotation angle. Rotation transforms the position of points in space without altering the shape or size of the original figure.

Figure 2 illustrates the concept of rotation, showing how a point P_a moves to position P_b after a rotation by an angle θ around a reference point or center of rotation. This type of transformation is widely used in fields such as geometry, computer graphics, and robotics, and plays an essential role in representing and manipulating objects in three-dimensional space. The reference, cited [23], provides a solid foundation for understanding these geometric concepts.

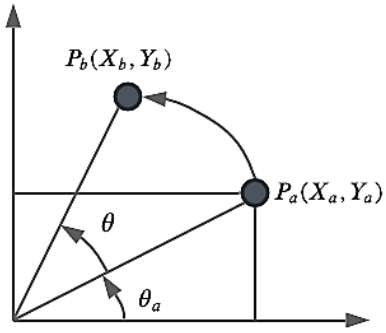

Figure 2. Rotation from point P_a to point P_b

The coordinates of point P_b with respect to point P_a are defined by (5), where X_a and Y_a are the components of the vector r as given in equation (6).

$$\begin{cases} X_b = X_a \cos\theta - Y_a \sin\theta \\ Y_b = Y_a \cos\theta + X_a \sin\theta \end{cases} \tag{5}$$

$$X_a = r \times \cos\theta \qquad Y_a = r \times \sin\theta \tag{6}$$

Thus, the final coordinates of a rotated image from point P_a to point P_b are represented in matrix form (7), also defined as the vector product $P_b = R \cdot P_a$, where R is the rotation matrix.

$$\begin{bmatrix} X_b \\ Y_b \\ 1 \end{bmatrix} = \begin{bmatrix} \cos\theta & -\sin\theta & 0 \\ \sin\theta & \cos\theta & 0 \\ 0 & 0 & 1 \end{bmatrix} \begin{bmatrix} X_a \\ Y_a \\ 1 \end{bmatrix} \tag{7}$$

where X_a, Y_a are the coordinates of the point a, $\cos\theta$ and $\sin\theta$ are the rotation angles, and X_b, Y_b are the final coordinates of the rotated point b.

Scaling It is a simple and direct transformation. It consists of applying a scale factor that can expand or contract a point P_a to a point P_b, as shown in Figure 3. The scale depends on the factor s, defined in equation (8), and can be represented in the matrix form as $P_b = S \cdot P_a$, represented in (9).

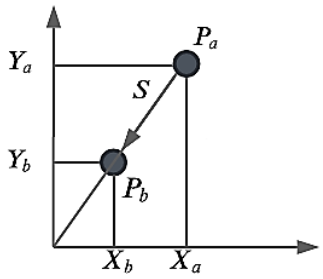

Figure 3. Scaling from point P_a to point P_b

$$X_b = S_x \cdot X_a \qquad Y_b = S_y \cdot Y_a \tag{8}$$

$$\begin{bmatrix} X_b \\ Y_b \\ 1 \end{bmatrix} = \begin{bmatrix} S_x & 0 & 0 \\ 0 & S_y & 0 \\ 0 & 0 & 1 \end{bmatrix} \begin{bmatrix} X_a \\ Y_a \\ 1 \end{bmatrix} \tag{9}$$

Theorem 1.1. affine matrix. The affine matrix is the result of combining translation, rotation, and scaling. [24] mentions that it is possible to apply several transformations simultaneously simply by concatenating them. The representation in a general form (10), results in a two-dimensional matrix called the affine matrix (11), which includes translation, rotation, and scaling.

$$\begin{bmatrix} X_b \\ Y_b \\ 1 \end{bmatrix} = \begin{bmatrix} 1 & 0 & t_x \\ 0 & 1 & t_y \\ 0 & 0 & 1 \end{bmatrix} \begin{bmatrix} \cos\theta & -\sin\theta & 0 \\ \sin\theta & \cos\theta & 0 \\ 0 & 0 & 1 \end{bmatrix} \begin{bmatrix} S_x & 0 & 0 \\ 0 & S_y & 0 \\ 0 & 0 & 1 \end{bmatrix} \begin{bmatrix} X_a \\ Y_a \\ 1 \end{bmatrix} \tag{10}$$

$$\begin{bmatrix} X_b \\ Y_b \\ 1 \end{bmatrix} = \begin{bmatrix} S_x \times \cos\theta & -S_y \times \sin\theta & t_x \\ S_x \times \sin\theta & S_y \times \cos\theta & t_y \\ 0 & 0 & 1 \end{bmatrix} \begin{bmatrix} X_a \\ Y_a \\ 1 \end{bmatrix} \tag{11}$$

where X_a, Y_a are the coordinates of the point a, t_x and t_y are the translation factors S_x, S_y are the scaling factors, $\sin\theta$, $\cos\theta$ are the rotation angles, and X_b, Y_b are the final coordinates of the point b.

3. Method

To locate the zero point of the workpiece, it is necessary to transform the machine coordinate system (MCS) into WCS, as illustrated in Figure 4.

The proposed method achieves this employing a computer vision algorithm ($CV - WCS$) that involves several steps, such as data acquisition, signal processing, feature extraction, image comparison, and the application of an affine matrix to locate the workpiece WCS. Initially, curve geometry calibration pieces are used for data collected using the $CV - WCS$ algorithm and then processed to remove noise and foreign artifacts in the

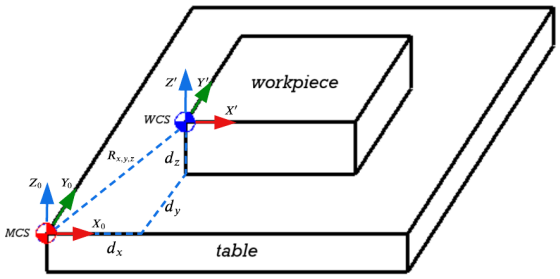

Figure 4. Translation of the machine coordinate system to the work coordinate system.

images. The resulting image is used to compare with an image reference called $GroundTruth$ (GT) for determining the WCS point location. The proposed method has the potential to significantly improve repeatability and reduce the time required for WCS localization, which is vital for various applications in precision machining.

3.1. Algorithm development

The design of the $CV-WCS$ algorithm is based on image processing to evaluate and compare geometric figures against a standard reference GT. This process is developed through the combination of five stages shown in Figure 5.

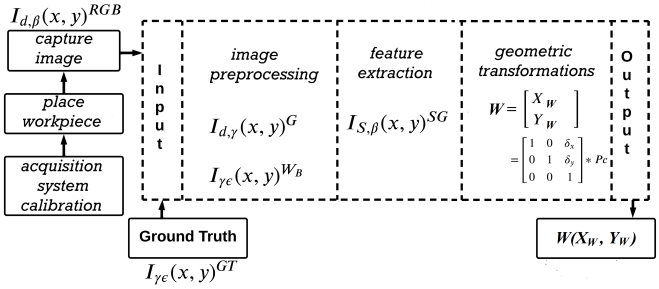

Figure 5. Design of the $CV-WCS$ algorithm

The $CV-WCS$ involves the following sequence:

Stage 1: Acquisition and processing of images of the parts to be machined. During this process, images are converted from the RGB format to grayscale and then to binary format.

Stage 2: Extraction of geometric features using the *Cany* algorithm to represent shapes in terms of the contour profile, facilitating identification and characterization of shape differences.

Stage 3: Performing geometric transformations based on the variation between the pixels of the reference image GT and the image of the real part to determine the displacement coordinates between the reference GT ($W_{c(x,y)}$) and the WCS of the part to be manufactured.

3.2. Calibration procedure for the image acquisition system

Before implementing the $CV-WCS$ algorithm, it is necessary to mount and calibrate a camera for the image acquisition system. Therefore, a calibration procedure based on [25] is carried out to determine the intrinsic parameters K_u, k_v, u_0, and v_0 to be substituted into the intrinsic matrix C_k, expressed in (12), to define the adjustment coordinates for the 3D positioning of the camera on the HAAS VF1 CNC milling machine for image capture, which will serve as input for the algorithm $CV-WCS$.

$$C_k = \begin{bmatrix} k_u & 0 & u_0 \\ 0 & k_v & v_0 \\ 0 & 0 & 1 \end{bmatrix} \tag{12}$$

where: k_u is the horizontal focal distance of the lens in millimeters (X-axis), k_v is the vertical focal distance of the lens in millimeters (Y-axis), and $[u_0, v_0]$ are the coordinates of the center of the image in pixels.

To carry out the calibration process, a chessboard calibration pattern is designed, which consists of squares distributed uniformly at a predefined distance shown in Figure 6.

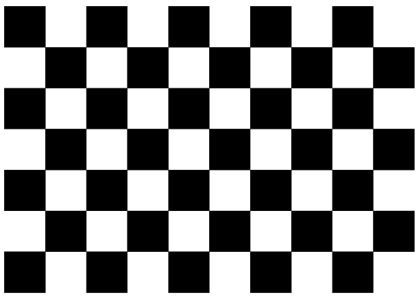

Figure 6. Calibration pattern

Based on the recommendation of [26], it was decided to use a chessboard printed on adhesive paper and affixed to a rectangular piece measuring 100.00 x 127.00 mm to prevent bending and warping. The pattern format consists of an even number (4) of squares along the Y-axis and an odd number (5) of squares along the X-axis. The size of each square is 23.00 mm.

Camera mounting: the camera is mounted on the top of the *CNC* machine on a rigid column as shown in Figure 7, positioned perpendicular to the work table and parallel to the calibration pattern to eliminate vibration and distortion.

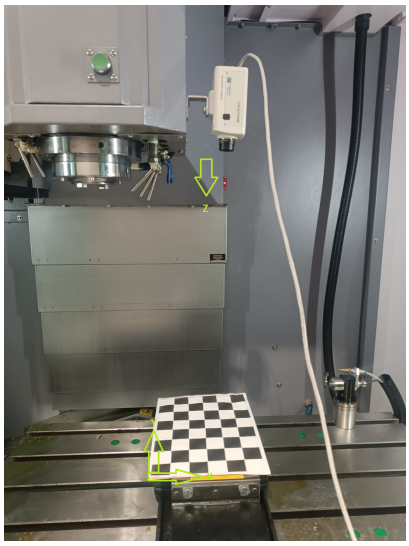

Figure 7. Camera calibration

Calibration procedure: Following [27], three calibration tests were performed, each with 12 images of the pattern in varying positions and orientations, yielding 36 images in total. Tables 1, 2, and 3 present the corresponding camera coordinates relative to the *MCS*.

Table 1. Calibration 1: current machine positions respect to the *MCS* on Haas VF1 milling machine

Test	X	Y	Z
1	-215.261	31.705	300.00
2	-215.261	38.205	300.00
3	-215.261	39.005	300.00
4	-215.261	36.305	300.00
5	-215.261	35.505	300.00
6	-215.261	34.405	300.00
7	-214.161	37.705	300.00
8	-213.461	37.005	300.00
9	-212.461	37.705	300.00
10	-216.361	37.705	300.00
11	-217.361	37.705	300.00
12	-218.361	37.705	300.00

Table 2. Calibration 2: current machine positions respect to the *MCS* on Haas VF1 milling machine

Test	X	Y	Z
1	-218.161	20.505	275.00
2	-218.161	25.405	275.00
3	-218.161	27.105	275.00
4	-218.161	30.205	275.00
5	-218.161	35.605	275.00
6	-218.161	36.605	275.00
7	-215.26	36.605	275.00
8	-218.161	38.605	275.00
9	-222.061	36.605	275.00
10	-224.061	36.605	275.00
11	-227.861	36.605	275.00
12	-213.161	36.605	275.00

Table 3. Calibration 3: current machine positions respect to the *MCS* on Haas VF1 milling machine

Test	X	Y	Z
1	-215.261	36.605	266.00
2	-215.261	37.705	266.00
3	-215.261	39.305	266.00
4	-215.261	34.205	266.00
5	-215.261	32.205	266.00
6	-215.261	32.205	266.00
7	-220.461	36.605	266.00
8	-218.761	36.605	266.00
9	-212.461	36.605	266.00
10	-208.261	36.605	266.00
11	-206.961	36.605	266.00
12	-204.961	36.605	266.00

Determination of calibration parameters: To compensate lens distortion, the Matlab application *Camera Calibrator* was employed, as illustrated in Figure 8. This tool implements the algorithm proposed by [28] to estimate the extrinsic parameters of the camera.

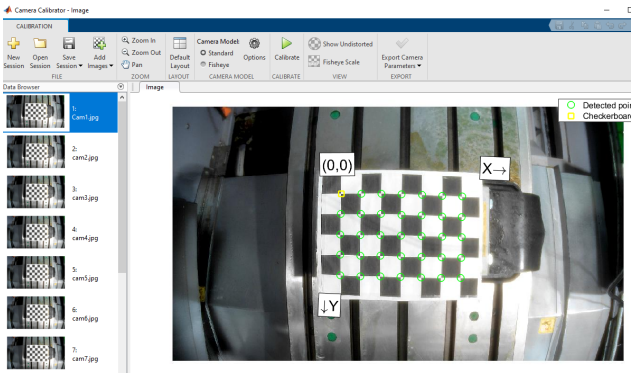

Figure 8. App Camera Calibrator: Source Matlab

Calibration results: The projection errors obtained in each calibration test are presented in Figures 9, 10, and 11. Among the three tests, Test 3 yielded the lowest projection errors; therefore, its calibration parameters were selected as the final values for the camera. The mean projection error in Test 3 was 0.28 pixels, which falls within the acceptable range of less than one pixel as defined by [28]. Figure 11 illustrates these results, highlighting session 11 as having the lowest projection error and session 4 as having the highest. Based on this calibration, the camera position was determined as $X = -206.961$, $Y = 36.605$, $Z = 266.0$ relative to the workpiece on the CNC machine. The final intrinsic camera parameters are summarized in Table 4.

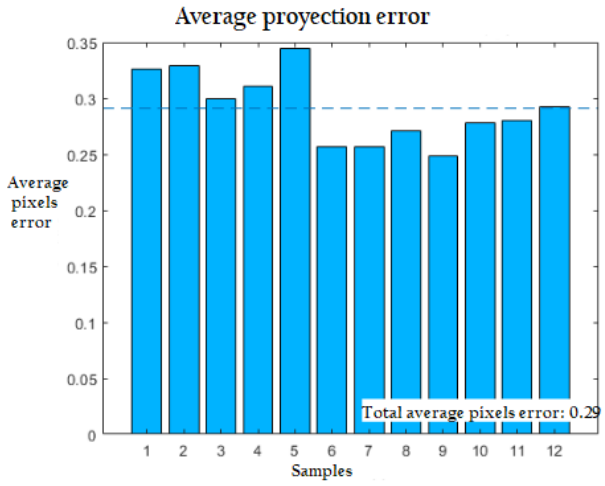

Figure 9. Average projection error: calibration test 1

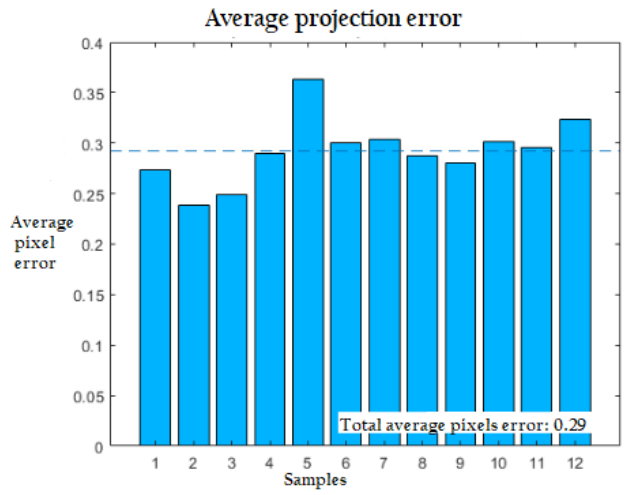

Figure 10. Average projection error: calibration test 2

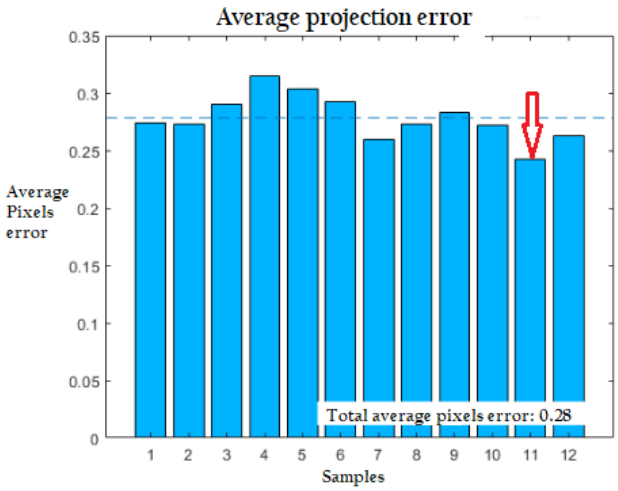

Figure 11. Average projection error: calibration test 3

Table 4. Camera calibration parameters

Parameter	Value
Focal length (pixels)	$[3160.2224 \pm 494.6915]$
Principal points (pixels)	$[564.4209 \pm 1.1462]$
Radial distortion	$[-11.3057 \pm 3.6534]$

3.3. Design of reference geometry

The initial phase of the methodology focuses on the design of the reference geometry called Ground Truth (GT). The GT for the geometry of the curve represents a binary image of the theoretically exact real part defined as $I_{d,\beta}(x,y)^{GT}$ as shown in Figure 12. This geometry was chosen based on the recommendation of [29], which identifies them as the basic forms that comprise the profile of any geometric figure.

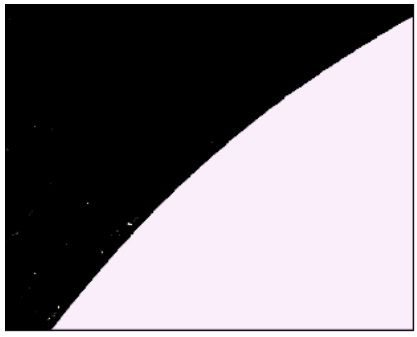

Figure 12. GT for curved geometry: $I_{d,C}(x,y)^{GT}$

After establishing GT, the position of the reference coordinate system of the defined GT, denoted as $W_{GT}(x,y)$, is determined in relation to the global coordinates (u,v), as shown in Figure 13. The location

of W_{GT} for the geometry of the curve was set at the coordinates (107, 480) in pixels.

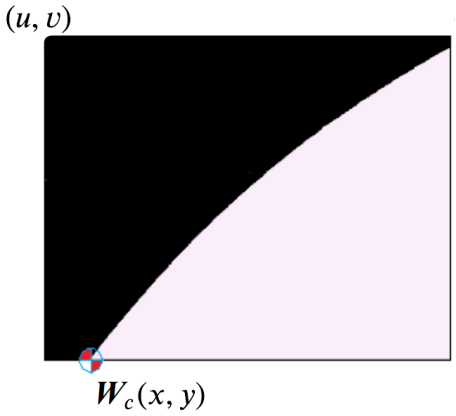

Figure 13. WCS_{GT} for curved, straight, and sloped geometries

Once the coordinates of $W_{GT(x,y)}$ are defined for the geometry of the curve according to its objective function $I_{d,\beta}(x,y)^{GT}$, the image capture process of the parts arranged on the HAAS VF1 milling machine begins.

3.4. Image acquisition

The image acquisition system for the HAAS VF1 milling machine consists of a computer, an acquisition board, and an IP HIKVISION camera mounted on the machine column. The camera, positioned perpendicular to the table and parallel to the workpiece (Figure 14), captures images at a resolution of 640 × 480 pixels. Images are transmitted via Ethernet with a fixed IP, stored in a designated folder, and processed by the *CV-WCS* algorithm. The captured images, in RGB format $I_{d,\beta}(x,y)^{RGB}$ as shown in Figure 15.

Figure 14. Part setup on HAAS VF1 milling machine

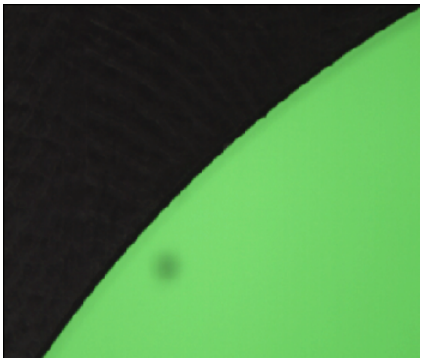

Figure 15. Image capture: $I_{d,C}(x,y)^{RGB}$

3.5. Image processing

Image processing constitutes the first stage of the *CV-WCS* method, enabling the enhancement and refinement of captured images. In this step, spatial filters are applied, including smoothing with $\sigma = 1.5$ and a Gaussian filter with $\epsilon = 1.5$, to improve image quality and repeatability prior to contour feature extraction as shown in Figure 16. These parameters were empirically determined through iterative testing on representative workpiece geometries, balancing noise reduction with material color and brightness. Subsequently, *CV-WCS* performs image segmentation to suppress noise and isolate regions of interest. In the initial segmentation phase, the original image $I_{d,\beta}(x,y)^{RGB}$ is converted into its grayscale representation $I_{d,\gamma}(x,y)^{G}$ using the function $rgb2gray(I_{d,\gamma})$, thereby reducing dimensionality from three channels to one.

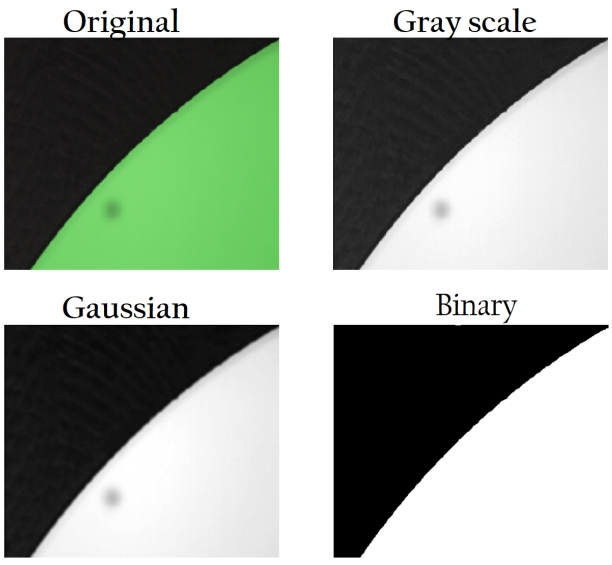

Figure 16. Image processing

3.6. Profile contour extraction

The second stage is dedicated to the extraction of the profile contour that describes the form present in the processed images. In this process, the algorithm performs a transformation of the binary image $I_{S,\beta}(x,y)^B$ into a 2D representation called a "*signature*," defined as the function $I_{S,\beta}(x,y)^{SG}$. This transformation is achieved through the application of the $cv2.findContours(I_{d,\gamma})$ algorithm, specifically designed for edge and corner detection, identifying changes and corners in the shapes present in the images.

3.7. Profile centroid calculation

The centroid C_S of a contour profile is calculated using the centroids equation (13). The resulting coordinates $C_S(X_c, Y_c)$ are then compared with the GT centroid X_G, Y_G previously defined using the coordinates of the discrete points in the profile k_n.

$$C_{S,\beta}, X_c = \frac{1}{n}\sum_{k=0}^{n-1} X_i(k), \quad C_{S,\beta}, Y_c = \frac{1}{n}\sum_{k=0}^{n-1} Y_i(k) \tag{13}$$

where:

- X_c is the X coordinate of the centroid.
- Y_c is the Y coordinate of the centroid.
- n is the total number of points in the profile.

The centroid $C_{S,\beta}, (X_c, Y_c)$ allows us to visualize the shape variations in the regions of interest within the $r(n)$ points, as shown in Figure 17, which is essential for the location of WCS.

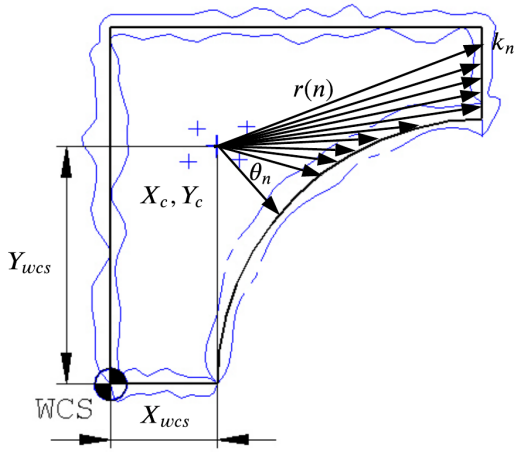

Figure 17. Profile centroid

3.8. WCS coordinates calculation

In the third step, the algorithm $CV - WCS$ calculates the adjustment coordinates δx and δy by computing the centroid differences of each signature with respect to its corresponding GT defined by equations (14) and (15).

$$\delta x = C_{S,\beta}(X) - C_{GT,\beta}(X) \tag{14}$$

$$\delta y = C_{S,\beta}(Y) - C_{GT_\beta}(Y) \tag{15}$$

where δx and δy are the values of the adjustment coordinates concerning the image world coordinates along the u and v axes in the camera reference coordinate system ($CRCS$).

Finally, the $CV - WCS$ algorithm uses the matrix (16) to translate WCS of the image with respect to MCS, as illustrated in Figure 18.

$$WCS = \begin{bmatrix} X_{WCS} \\ Y_{WCS} \\ 1 \end{bmatrix} = \begin{bmatrix} 1 & 0 & X_{RCTS} \\ 0 & 1 & Y_{RCTS} \\ 0 & 0 & 1 \end{bmatrix} \begin{bmatrix} d_x \\ d_y \\ 1 \end{bmatrix} \tag{16}$$

where d_x and d_y represent the distances from MCS to the calibration point, X_{RCTS} and Y_{RCTS} are the reference coordinate tool system ($RCTS$) and X_W, Y_W are the coordinates of the workpiece WCS.

Figure 18 shows the translation process from MCS to WCS

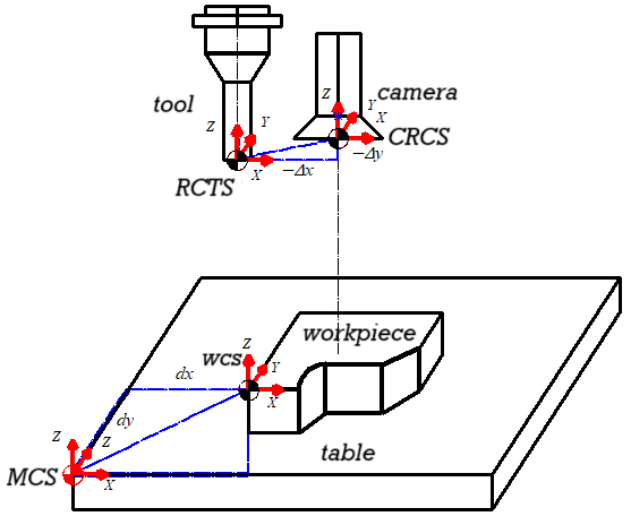

Figure 18. Coordinate translation to the WCS on the HAAS VF1 milling machine

4. Results

4.1. Image acquisition results

The first stage of image analysis involves the acquisition of geometries; a total of 37 images were captured. Figure 19 shows a selection of 20 captured images corresponding to the function $I_{d,C}(x,y)^{RGB}$, which represents the curved geometry. The captured images cover a variety of conditions, including different perspectives and lighting angles, reflecting the diversity of situations.

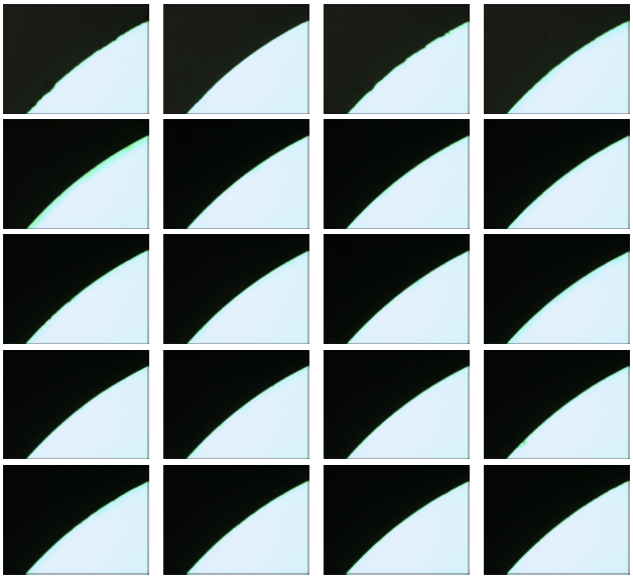

Figure 19. images acquisition of the curved geometry

4.2. Contour profiles obtained from curved geometries

Once the RGB images were captured, in the second stage, the $CV-WCS$ algorithm applied image processing techniques to transform the function $I_{d,\beta}(x,y)^{RGB}$ into binary format $I_{d,\beta}(x,y)^{RGB}$ to extract the geometry properties and convert them into the function $I_{S,C}(x,y)^{SG}$. As a result of this process, 37 profile contours corresponding to the geometry of the curve were extracted with image quality. Figure 20 shows the results of the extraction of profile contours of a curve corresponding to the Sg1-31 to Sg1-36 samples:

4.3. Results of coordinate offset values

The coordinate offset values were derived from the differences in the centroids $M_{\delta\beta}(k)$ of $I_{S,C}(x,y)^{SG}$ and GT. Table 5 presents the offset values in pixels, δx and δy, corresponding to the curved, straight, and sloped geometries, respectively, as generated by the $CV-WCS$ algorithm.

Table 5. Offset values of the curved geometry

S1	δx	δy	S2	δx	δy
1	-0.444	-1.124	20	2.031	1.559
2	-15.335	-0.990	21	1.772	1.408
3	-15.164	-0.670	22	-0.005	0.282
4	1.760	0.776	23	2.371	1.147
5	1.156	0.460	24	1.541	1.993
6	2.063	0.875	25	1.317	1.388
7	0.962	0.762	26	0.753	0.238
8	2.085	1.001	27	1.152	1.974
9	0.007	-0.315	28	0.764	1.242
10	2.036	0.671	29	0.118	1.498
11	1.387	1.391	30	1.535	1.976
12	1.729	0.745	31	1.520	1.959
13	0.593	0.151	32	1.678	1.782
14	0.092	0.545	33	1.511	1.192
15	1.462	1.400	34	2.637	1.808
16	-0.603	1.228	35	-1.131	0.671
17	0.571	1.445	36	1.341	1.032
18	0.930	1.572	37	0.237	1.559
19	-0.703	0.534			

4.4. Workpiece WCS calculation

The algorithm uses the offset values (δx and δy) to translate the reference coordinate of the tool system ($RCTS$), applying the matrix (17). The 0.127 factor is used to convert the pixel units to millimeter units according to the image resolution employed by the camera. The coordinates of $RCTS$ are adjusted by applying the displacement factors $-\Delta_x = -30.00$ mm and $-\Delta_y = -10.0$ mm, which are determined from the central reference position of the camera lens to the central reference position of the tool.

$$RCTS = \begin{bmatrix} X_W \\ Y_W \\ 1 \end{bmatrix} = \begin{bmatrix} -\Delta_x \\ -\Delta_y \\ 1 \end{bmatrix} \begin{bmatrix} 1 & 0 & 0.127\delta_x \\ 0 & 1 & 0.127\delta_y \\ 0 & 0 & 1 \end{bmatrix} \tag{17}$$

Then, the $CV-WCS$ algorithm performs the final translation from $RCTS$ to the new WCS concerning MCS, applying the translation matrix (18). The coordinate values: $X_{W_L} = 89.857$ mm and $Y_{W_L} = 270.086$ mm extracted from Table 6 are the results of the application of the translation matrix to the sample SG1-35:

$$WCS = \begin{bmatrix} X_W \\ Y_W \\ 1 \end{bmatrix} = \begin{bmatrix} 1 & 0 & -30.143 \\ 0 & 1 & -9.914 \\ 0 & 0 & 1 \end{bmatrix} \begin{bmatrix} 120.00 \\ 280.00 \\ 1 \end{bmatrix} \tag{18}$$

The displacement coordinate values $d_x = 120.00$ mm and $d_y = 280.00$ mm were determined by measuring the position of $RCTS$ relative to MCS.

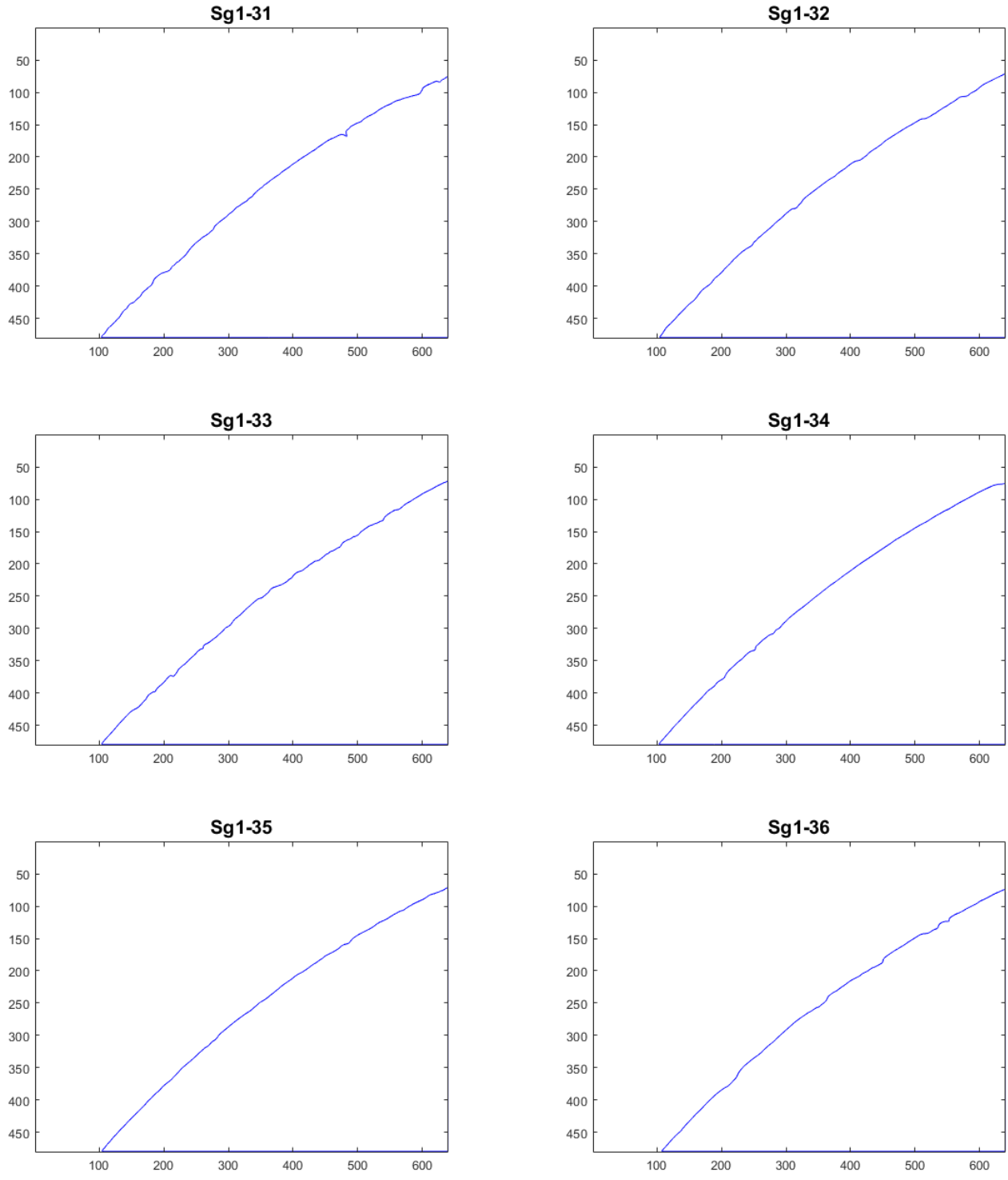

Figure 20. Contour profiles of curved geometry: samples Sg1-31 to Sg1-36 (units: pixels)

The summary of the calculated WCS coordinates is shown in millimeters in Table 6 as the output values of the algorithm for each geometry.

4.5. Evaluation of repeatability in determining the workpiece WCS coordinates

To evaluate whether the $CV-WCS$ algorithm improves repeatability in locating the zero coordinates

Table 6. WCS coordinate values in millimeters relative to the MCS

M1	X_{WCS}	Y_{WCS}	M2	X_{WCS}	Y_{WCS}
1	89.429	268.749	20	91.904	271.432
2	74.538	268.883	21	91.645	271.281
3	74.710	269.204	22	89.869	270.155
4	91.633	270.649	23	92.244	271.020
5	91.029	270.333	24	91.414	271.866
6	91.936	270.748	25	91.190	271.261
7	90.835	270.635	26	90.626	270.111
8	91.958	270.874	27	91.025	271.847
9	89.880	269.558	28	90.637	271.115
10	91.909	270.544	29	89.991	271.371
11	91.260	271.264	30	91.408	271.849
12	91.602	270.618	31	91.393	271.832
13	90.466	270.024	32	91.551	271.655
14	89.965	270.418	33	91.384	271.065
15	91.335	271.273	34	92.510	270.959
16	89.270	271.101	35	89.857	270.086
17	90.444	271.318	36	91.214	270.905
18	90.803	271.445	37	90.110	271.432
19	89.171	270.407			

of the workpiece on the HAAS VF1 three-axis milling machine CNC, first, uncertainty tests were performed to determine the error in locating the center of a drilled hole, comparing the repeatability of two methods with the Wireless intuitive probing system ($WIPS$) and the edge finder. The procedure for evaluating repeatability consists of determining the position of the center of a drilled hole in the prototype workpiece regarding the reference planes A and B, as shown in Figure 21.

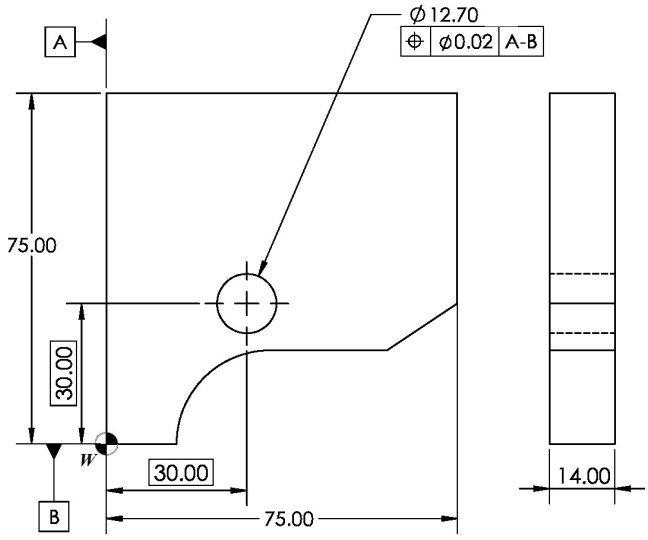

Figure 21. Measurement reference drawing

Five measurements of the center position of the hole were taken based on the basic distances (30,30), measured from the WCS using a CMM for each method. The position error in locating the hole center relative to WCS of the workpiece is evaluated for each method, using the range of 30 ± 0.02 mm with a confidence interval of approximately 68.3% as recommended by [30].

The position errors of each zero-point localization method of each piece of work are calculated using the following equations: mean error (μ_E), standard deviation of errors (σ_e) and uncertainty u_m, as described in equations (19), (20), (21) and (22), respectively. A coverage factor of $k = 2$ is used to achieve a confidence level of 95%. The uncertainty results are presented in Tables 7, 8, and 9, for the X and Y axes, respectively.

$$\mu_e(X) = \frac{\sum_{i=1}^{n} \text{Error}_i^X}{n} \qquad \mu_e(Y) = \frac{\sum_{i=1}^{n} \text{Error}_i^Y}{n} \tag{19}$$

$$\sigma_e(X) = \sqrt{\frac{\sum_{i=1}^{n} (\text{Error}_i^X - \overline{\text{Error}^X})^2}{n-1}} \tag{20}$$

$$\sigma_e(Y) = \sqrt{\frac{\sum_{i=1}^{n} (\text{Error}_i^Y - \overline{\text{Error}^Y})^2}{n-1}} \tag{21}$$

$$u_m(X) = K \times \sigma_e(X) \qquad u_m(Y) = K \times \sigma_e(Y) \tag{22}$$

Table 7. Uncertainty results for the *WIPS* method

Workpiece	X (mm)	Y (mm)	Error (mm)
1	30.000	30.000	(0.000, 0.000)
2	30.010	30.010	(0.010, 0.010)
3	29.990	29.990	(-0.010, -0.010)
4	30.000	30.020	(0.000, 0.020)
5	30.010	29.980	(0.010, -0.020)
μ_E	(0.002, 0.002)		
σ_e	(0.004, 0.012)		
u_m	(0.008, 0.024)		

The results obtained show that the uncertainty in measuring the location of the hole center, relative to the reference coordinates, for the $WIPS$ and $CV - WCS$ methods exhibits a low dispersion of the measured positions around the expected theoretical or nominal position. This indicates that both methods produce a combined uncertainty of 0.026 mm in the X axis and 0.034 mm in the Y axis, according to the Law of Propagation of Uncertainty by Gauss described in [31].

Similarly, the $edgefinder$ show relatively low measurement uncertainty in locating the hole center,

Table 8. Uncertainty results for the *edge finder* method

Workpiece	X (mm)	Y (mm)	Error (mm)
1	30.030	30.020	(0.030, 0.020)
2	29.970	30.030	(-0.030, 0.030)
3	30.010	29.970	(0.010, -0.030)
4	30.020	29.980	(0.020, -0.020)
5	29.980	30.010	(-0.020, 0.010)
μ_E	(0.002, 0.002)		
σ_e	(0.020, 0.020)		
u_m	(0.040, 0.040)		

Table 9. Uncertainty results for the *VA-WCS* method

Workpiece	X (mm)	Y (mm)	Error (mm)
1	30.020	30.010	(0.020, 0.010)
2	29.980	30.020	(-0.020, 0.020)
3	30.000	29.980	(0.000, -0.020)
4	30.010	30.000	(0.010, 0.000)
5	29.990	29.990	(-0.010, -0.010)
μ_E	(0.000, 0.000)		
σ_e	(0.012, 0.012)		
u_m	(0.024, 0.024)		

although slightly higher than that observed with the $WIPS$ and $CV-WCS$ methods, with a combined uncertainty of 0.075 mm in both the X and Y axes.

4.6. Comparative discussion with related works

Finally, the uncertainty results were compared with two AI/vision-based localization methods. The first is the cloud-based approach for the automatic origin of the workpiece (CCS) proposed by [1], which achieves a mean absolute percentage error of 0.007. The second is the automatic part localization in a machine coordinate system using a 3D laser scaner ($3DScan$) proposed by [32], which reports a positional error of ±0.015 in. Both methods rely on computer vision to determine the WCS in three-axis milling machines. Unlike these previous approaches, the CCS method employs a stereo camera system mounted directly on the machine spindle, and the $3DScan$ method was mounted in a custom-built assembly and suspended from an aluminum beam bolted to the HAAS machining center, they presents a vibration effect.

After the uncertainty tests, repeatability was evaluated to determine whether the CV-WCS method provides a consistent WCS localization compared to other methods.

To determine the acceptable repeatability of each method, the standard deviation of the positional errors of the hole centers along the X and Y axes was calculated, based on the recommendations of [33] and [34], which suggest an acceptable range between 0.001 and 0.010 mm. Table 10 presents the repeatability results for each method.

Table 10. Repeatability of each method for locating the workpiece zero coordinates.

Method	$\sigma_e(X)$ **(mm)**	$\sigma_e(Y)$ **(mm)**
CCS	0.007	0.007
$CV-WCS$	0.012	0.012
$3DScan$	0.015	0.015
$WIPS$	0.008	0.016
$edgefinder$	0.020	0.020

These results suggest that for applications where repeatability is a critical factor, the CCS method is the most suitable, followed by the $CV-WCS$ method and the $3DScan$ method.

4.7. Limitations of the CV-WCS

The proposed solution only applies to a three-axis machining center, and to increase the generality of the proposal, it will be necessary to apply it to other machines in future studies.

The development of the CV-WCS algorithm for the localization of WCS in CNC milling processes is limited to laboratory experimental validation, scheduled between August 2023 and September 2024. Furthermore, the implementation of CV-WCS for error reduction in the setup of WCS is restricted to three-axis machining centers, where it functions as a support tool for CNC operators and technicians, enabling them to perform setup tasks efficiently, in minimal time and with a reduced likelihood of errors.

4.8. Advantages of the CV-WCS

The proposed $CV\check{}WCS$ method offers a vision-based alternative for localizing the WCS on CNC milling machines with several key distinctions from existing approaches. Unlike spindle-mounted systems, the camera is mounted on the machine column, eliminating interference with the tool path and simplifying integration. On-machine processing allows all computations to be performed locally, reducing latency and avoiding reliance on cloud-based systems. This configuration not only automates WCS identification, cutting setup time to approximately 1.820 seconds, but also enhances repeatability with uncertainty levels comparable to commercial probing systems such as WIPS. The non-contact measurement minimizes tool and workpiece

wear, while automated algorithms reduce operator-dependent errors. Additionally, the method is flexible across diverse geometries, cost-effective through low-cost hardware and open-source software, and aligns with Industry 4.0 objectives by supporting integration with digital twins, adaptive control, and cloud-based monitoring for autonomous machining environments.

4.9. Future research directions

Future work will focus on improving the robustness and applicability of the proposed *CV-WCS* method. Key directions include improving resilience to lighting and environmental variations, extending the applicability to multi-axis machines, and integrating deep learning approaches such as Faster R-CNN for feature detection under challenging conditions [35, 36]. Further efforts will target algorithm optimization for real-time execution on *CNC* controllers, generalization to diverse workpiece geometries and materials, and large-scale industrial validation. Finally, integration with Industry 4.0 frameworks, including digital twins and adaptive process control, will support the fully autonomous transition of setup and machining operations.

5. Conclusions and discussions

In conclusion, the implementation of the $CV-WCS$ method for the localization of the workpiece WCS with geometry curve pieces mounted on the HAAS VF1 three-axis milling machine represents a significant advance in optimizing the initial setup of the machining processes. The $CV-WCS$ method demonstrates the ability to employ image processing techniques and geometry transformations to improve repeatability in the real-time localization of the WCS on parts mounted on the milling machine table.

Acknowledgement

This research was partially supported by the Technological University of Chihuahua, which provided access to its laboratory facilities, and by SECIHTI (Secretaría de Ciencia, Humanidades, Tecnología e Innovación) Mexican goberment through funding support.

References

[1] de Araujo, P.R.M. and Lins, R.G. (2021) Cloud-based approach for automatic cnc workpiece origin localization based on image analysis. *Robotics and Computer-Integrated Manufacturing* **68**: 102090. URL https://doi.org/10.1016/j.rcim.2020.102090.

[2] Chen, Y., Gunraj, H., Zeng, E.Z., Meyer, R., Gilles, M. and Wong, A. (2023) Mmrnet: Improving reliability for multimodal object detection and segmentation for bin picking via multimodal redundancy. In *2023 IEEE/CVF Conference on Computer Vision and Pattern Recognition Workshops (CVPRW)*: 68–77. URL https://doi.org/10.1109/CVPRW59228.2023.00012.

[3] Ruijiao Yin, J.Y. (2019) Research on robot control technology based on vision localization. *Journal on Artificial Intelligence* **1**(1): 37–44. URL http://www.techscience.com/jai/v1n1/29010.

[4] Xiong, Z., Chu, Y., Liu, G. and Li, Z. (2001) Workpiece localization and computer aided setup system. In *Proceedings 2001 IEEE/RSJ International Conference on Intelligent Robots and Systems. Expanding the Societal Role of Robotics in the the Next Millennium (Cat. No.01CH37180)*, **2**: 1141–1146 vol.2. URL https://doi.org/10.1109/IROS.2001.976322.

[5] Zhu, W., Qin, Z., Wang, P. and Qiao, H. (2013) Model-based work-piece localization with salient feature selection. In *2013 IEEE International Conference on Robotics and Biomimetics (ROBIO)*: 493–497. URL https://doi.org/10.1109/ROBIO.2013.6739508.

[6] Li, Z., Sato, R., Shirase, K. and Sakamoto, S. (2021) Study on the influence of geometric errors in rotary axes on cubic-machining test considering the workpiece coordinate system. *Precision Engineering* **71**: 36–46. URL https://doi.org/10.1016/j.precisioneng.2021.02.011.

[7] Torres-Medina, Y. (2020) El análisis del error humano en la manufactura: un elemento clave para mejorar la calidad de la producción. *Revista UIS Ingenierías* **19**(4): 53–62. URL https://doi.org/10.18273/revuin.v19n4-2020005.

[8] Soori, M., Arezoo, B. and Habibi, M. (2013) Dimensional and geometrical errors of three-axis cnc milling machines in a virtual machining system. *Computer-Aided Design* **45**(11): 1306–1313. URL https://doi.org/10.1016/j.cad.2013.06.002.

[9] Grisales-Grisales, N., Durango-Idárraga, S., Álvarez-Vargas, C.A. and Flórez-Hurtado, R.D. (2020) Calibración cinemática de una ruteadora cnc usando un modelo cuasi-estático de error y fotogrametría monocular. *Revista UIS Ingenierías* **19**(3): 15–30. URL https://doi.org/10.18273/revuin.v19n3-2020002.

[10] Báez, Y.A., Rodríguez, M.A., De la Vega, E.J. and Tlapa, D.A. (2013) Factores que influyen en el error humano de los trabajadores en líneas de montaje manual. *Información tecnológica* **24**(6): 67–78. URL https://doi.org/10.4067/S0718-07642013000600010.

[11] Popov, K., Dimov, S., Ivanov, A., Pham, D.T. and Gandarias, E. (2010) New tool-workpiece setting up technology for micro-milling. *The International Journal of Advanced Manufacturing Technology* **47**(1): 21–27. URL https://doi.org/10.1007/s00170-009-2055-2.

[12] XuYi, Ma, L. and Li, Z. (2008) A geometric algorithm for symmetric workpiece localization. In *2008 7th World Congress on Intelligent Control and Automation*: 6065–6069. URL https://doi.org/10.1109/WCICA.2008.4592864.

[13] Setti, A., Bosetti, P. and Ragni, M. (2016) Artool-augmented reality platform for machining setup and maintenance. In *Proceedings of SAI Intelligent Systems Conference* (Springer): 457–475. URL https://doi.org/10.1007/978-3-319-56994-9_33.

[14] Gu, J., Agapiou, J.S. and Kurgin, S. (2015) Cnc machine tool work offset error compensation method. *Journal of Manufacturing Systems* **37**: 576–585. URL https://doi.org/10.1016/j.jmsy.2015.04.001.

[15] Xu, H.H. and Dai, C. (2014) Research on precision detection and error compensation technology for 3-axis cnc milling machine. *Applied Mechanics and Materials* **455**: 505–510. URL https://doi.org/10.4028/www.scientific.net/AMM.455.505.

[16] Zhang, J. (2018) Research on cnc lathe programming and improving machining accuracy. In *IOP Conference Series: Materials Science and Engineering* (IOP Publishing), **452**: 042050. URL https://doi.org/10.1088/1757-899X/452/4/042050.

[17] Martinova, L., Obukhov, A. and Sokolov, S. (2020) Practical aspects of ensuring accuracy of machining on cnc machine tools within framework of "smart manufacturing". In *2020 International Russian Automation Conference (RusAutoCon)* (IEEE): 898–902. URL https://doi.org/10.1109/RusAutoCon49822.2020.9208079.

[18] Salas-Arias, K.M., Madriz-Quirós, C.E., Sánchez-Brenes, O., Sánchez-Brenes, M. and Hernández-Granados, J.B. (2018) Factores que influyen en errores humanos en procesos de manufactura moderna. *Revista Tecnología en Marcha* **31**(1): 22–34. URL https://doi.org/10.18845/tm.v31i1.3494.

[19] Torres Diaz, C.A. (2019) Matrices y sistemas de ecuaciones lineales. *Repositorio Institucional* URL https://repositorioslatinoamericanos.uchile.cl/handle/2250/653643.

[20] Barrientos, A., Álvarez, M., Hernández, J.D., Del Cerro, J. and Rossi, C. (2012) *Modelado de Cadenas Cinemáticas mediante Matrices de Desplazamiento. Una alternativa al método de Denavit-Hartenberg* (Science Direct), **9**, 371–382. URL https://doi.org/10.1016/j.riai.2012.09.004.

[21] Diprasetya, M.R. and Schwung, A. (2022) Homogeneous transformation matrix based neural network for model based reinforcement learning on robot manipulator. In *2022 IEEE International Conference on Industrial Technology (ICIT)* (IEEE): 1–6. URL https://doi.org/10.1109/ICIT48603.2022.10002834.

[22] Villamarín, D. (2015) Estado del arte, herramientas y aplicaciones para transformaciones geométricas 3d. In *Congreso de Ciencia y Tecnología ESPE*, **10**: 226–231. URL https://www.researchgate.net/publication/290964976_Estado_del_Arte_Herramientas_y_Aplicaciones_para_Transformaciones_geometricas_3D.

[23] Barrientos, A. *et al.* (2017) *Fundamentos de robótica* (Arquitectura e Ingeniería), **2**, 211–382. URL https://www.academia.edu/40692152/Fundamentos_de_Rob%C3%B3tica_A_Barrientos_L_Pe%C3%B1in_C_Balaguer_R_Aracil_2ed.

[24] Maldavsky, D. (1977) Teoría de las representaciones: sistemas y matrices, transformaciones y estilos. In *Teoría de las representaciones: sistemas y matrices, transformaciones y estilos* (Portal Regional BVS), 267–267. URL https://sibi.upn.mx/cgi-bin/koha/opac-detail.pl?biblionumber=96663.

[25] Meraz-Méndez, M., Muñoz-López, L.E., Reynoso-Jardón, E.L. and Corral-Ramírez, G. (2024) Camera calibration procedure for extracting form deviation features in machined parts through computer vision algorithms. *Journal of Mechanical Engineering* **8**(21): 1–e30821111.

[26] Jiao, J., Huang, C., Liu, H. and Zhang, G. (2018) A chinese chessboard calibration method in chess-playing robot by machine vision sensing. In *Journal of Physics: Conference Series* (IOP Publishing), **1026**: 012023. URL https://doi.org/10.1088/1742-6596/1026/1/012023.

[27] Mejia, J.B. and Varona, R.L. (2014) Calibración de cámara termográfica fluke ti-32. *Scientia et technica* **19**(1): 59–66.

[28] Zhang, Z. (2000) A flexible new technique for camera calibration. *IEEE Transactions on pattern analysis and machine intelligence* **22**(11): 1330–1334. URL https://doi.org/10.1109/34.888718.

[29] Yang, C. and Yu, Q. (2019) Multiscale fourier descriptor based on triangular features for shape retrieval. *Signal Processing: Image Communication* **71**: 110–119. URL https://doi.org/10.1016/j.image.2018.11.004.

[30] Bipm, I., IFCC, I. and IUPAC, I. (1995) Oiml 2008 evaluation of measurement data—guide to the expression of uncertainty in measurement. *Joint Committee for Guides in Metrology, Bureau International des Poids et Mesures, JCGM* **100**.

[31] International Organization for Standardization (2008), ISO/IEC Guide 98-3:2008 Uncertainty of measurement - Part 3: Guide to the expression of uncertainty in measurement (GUM:1995). Published (Edition 1, 2008). This standard was last reviewed and confirmed in 2023. Therefore this version remains current.

[32] Srinivasan, H., Harrysson, O. and Wysk, R. (2015) Automatic part localization in a cnc machine coordinate system by means of 3d scans. *International Journal of Advanced Manufacturing Technology* **81**: 1127–1138. doi:10.1007/s00170-015-7178-z, URL https://doi.org/10.1007/s00170-015-7178-z.

[33] Wallace, J. (2010) Ten methods for calculating the uncertainty of measurement. *Science & Justice* **50**(4): 182–186. doi:https://doi.org/10.1016/j.scijus.2010.06.003, URL https://www.sciencedirect.com/science/article/pii/S1355030610000705.

[34] Khusainov, R., Ziangirova, E. and Davletshina, G. (2020) Estimation of precision parameters of milling machines. In *IOP Conference Series: Materials Science and Engineering*, **915**: 012031. URL https://doi.org/10.1088/1757-899X/915/1/012031.

[35] Singh, K.D. and Singh, P.D. (2023) Machine learning in robotics with fog/cloud computing and iot. *EAI Endorsed Transactions on AI and Robotics* **2**. URL https://doi.org/10.4108/airo.3621.

[36] Zangana, H., Mustafa, R. and Omar, A. (2024) A hybrid approach for robust object detection: Integrating template matching and faster r-cnn. *EAI Endorsed Transactions on AI and Robotics* **3**. doi:10.4108/airo.6858, URL https://publications.eai.eu/index.php/airo/article/view/6858.